nature communications



Article

https://doi.org/10.1038/s41467-024-51878-6

Rigid covalent organic frameworks with thiazole linkage to boost oxygen activation for photocatalytic water purification

Received: 11 May 2024

Accepted: 21 August 2024

Published online: 27 August 2024

Check for updates

Yanghui Hou^{1,2,3,7}, Peng Zhou ^{⊕ 4,7}, Fuyang Liu ^{⊕ 1,2,3}, Ke Tong⁵, Yanyu Lu^{1,2,3}, Zhengmao Li^{1,2,3}, Jialiang Liang⁶ & Meiping Tong ^{⊕ 1,2,3} ⊠

Owing to their capability to produce reactive oxygen species (ROS) under solar irradiation, covalent organic frameworks (COFs) with pre-designable structure and unique architectures show great potentials for water purification. However, the sluggish charge separation, inefficient oxygen activation and poor structure stability in COFs restrict their practical applications to decontaminate water. Herein, via a facile one-pot synthetic strategy, we show the direct conversion of reversible imine linkage into rigid thiazole linkage can adjust the π -conjugation and local charge polarization of skeleton to boost the exciton dissociation on COFs. The rigid linkage can also improve the robustness of skeleton and the stability of COFs during the consecutive utilization process. More importantly, the thiazole linkage in COFs with optimal C 2p states (COF-S) effectively increases the activities of neighboring benzene unit to directly modulate the O₂-adsorption energy barrier and improve the ROS production efficiency, resulting in the excellent photocatalytic degradation efficiency of seven toxic emerging contaminants (e.g. degrading ~99% of 5 mg L⁻¹ paracetamol in only 7 min) and effective bacterial/algal inactivation performance. Besides, COF-S can be immobilized in continuous-flow reactor and in enlarged reactor to efficiently eliminate pollutants under natural sunlight irradiation, demonstrating the feasibility for practical application.

The emerging organic contaminants such as pharmaceuticals, personal care products, antibiotics, and endocrine-disrupting chemicals present in aquatic environments have recently drawn great attentions due to their potential risks to aquatic ecosystems and human health^{1,2}. To ensure water safety, advanced oxidation processes (AOPs) have been increasingly employed to eliminate emerging organic contaminants after the treatment via conventional biological process³. Owing to the use of naturally abundant sunlight as the sole energy

input, the photocatalysis has been regarded as one of the most sustainable, cost-effective and promising AOPs to remove organic pollutants from water^{4,5}. Comparing with metal-based photocatalysts that might potentially release metal ions into water and thus could produce secondary contamination⁶, metal-free photocatalysts, particularly carbon-based photocatalysts such as carbon dots⁷, carbon nanotubes⁸, reduced graphene⁹, and graphitic carbon nitride¹⁰ that would not cause the potential contamination of metal ions during their usage

¹College of Environmental Sciences and Engineering, Peking University, Beijing 100871, P. R. China. ²The Key Laboratory of Water and Sediment Sciences (Ministry of Education), Peking University, Beijing 100871, P. R. China. ³State Environmental Protection Key Laboratory of All Material Fluxes in River Ecosystems, Peking University, Beijing 100871, P. R. China. ⁴Eco-environment and Resource Efficiency Research Laboratory, School of Environment and Energy, Peking University Shenzhen Graduate School, Shenzhen, Guangdong 518055, P. R. China. ⁵School of Environmental Science and Engineering, TianGong University, Tianjin 300387, P. R. China. ⁶College of Environment and Ecology, Chongqing University, Chongqing 400045, PR China. ⁷These authors contributed equally: Yanghui Hou, Peng Zhou. ⊠e-mail: tongmeiping@pku.edu.cn

have drawn great attentions for water decontamination. Among various carbon-based photocatalysts. COFs (one of the novel metal-free photocatalysts) with customizable chemical structures and unique architectures recently have shown great potentials for the elimination of emerging organic contaminants in water owing to their capability to generate reactive species (e.g., $\cdot O_2^-$, $\cdot OH$, and h^+) under sunlight irradiation^{4,11,12}. However, the sluggish charge separation, inefficient oxygen activation, and poor structure stability of COFs during the reaction process yet constrain the photocatalytic efficiency and practical application^{13,14}. Owing to the simple crystallization process and controllable porosity, the imine-linked COFs exhibit promising applications in the field of photocatalysis, such as oxygen evolution reaction¹⁵, hydrogen evolution reaction¹⁶, and hydrogen peroxide photosynthesis¹⁷. Strategies such as heterojunction construction^{18,19}, single-atom incorporation²⁰, and suitable active-site modification²¹ have been shown to effectively improve the photocatalytic performance and stability of imine-linked COFs. However, these strategies often require multiple synthesis steps, which are complex, time and energy-consuming. Therefore, it is urgent to develop a facile and costeffective strategy to simultaneously improve the charge separation efficiency, oxygen activation capacity, and stability of COFs for the potential water decontamination in actual water, which yet remains a great challenge.

Herein, by converting the reversible imine linkage into rigid oxazole/thiazole linkage, the conventional imine-linked COFs (COF-A) are successfully transformed into oxazole/thiazole-linked COFs (COF-O and COF-S) via a facile one-pot synthetic strategy (Fig. 1a). Based on ultrafast spectroscopy experiments and theoretical calculations, we find that linking COFs by oxazole/thiazole linkages effectively modulates the exciton (e^--h^+ pair) dissociation behaviors on COFs by adjusting the π -conjugation and local charge polarization of skeleton. Comparing with the reversible imine linkage, the rigid oxazole/thiazole linkage in COFs also improves the robustness of the skeleton and the structure stability of COFs. Thiazole linkage in COF-S with optimal C 2p states effectively increases the activities of neighboring benzene units to modulate the O₂-adsorption energy barrier, resulting in the extraordinary degradation performance of paracetamol under visible-light irradiation. The degradation performance of COF-S in four real water samples and the degradation/inactivation performance towards different micropollutants (including other six organic contaminants, bacteria, and algae) are also explored. To further evaluate the feasibility of COF-S for practical application, the degradation performance of paracetamol in continuous-flow reaction system under visible-light irradiation, and in an enlarged reactor with natural sunlight irradiation is also investigated.

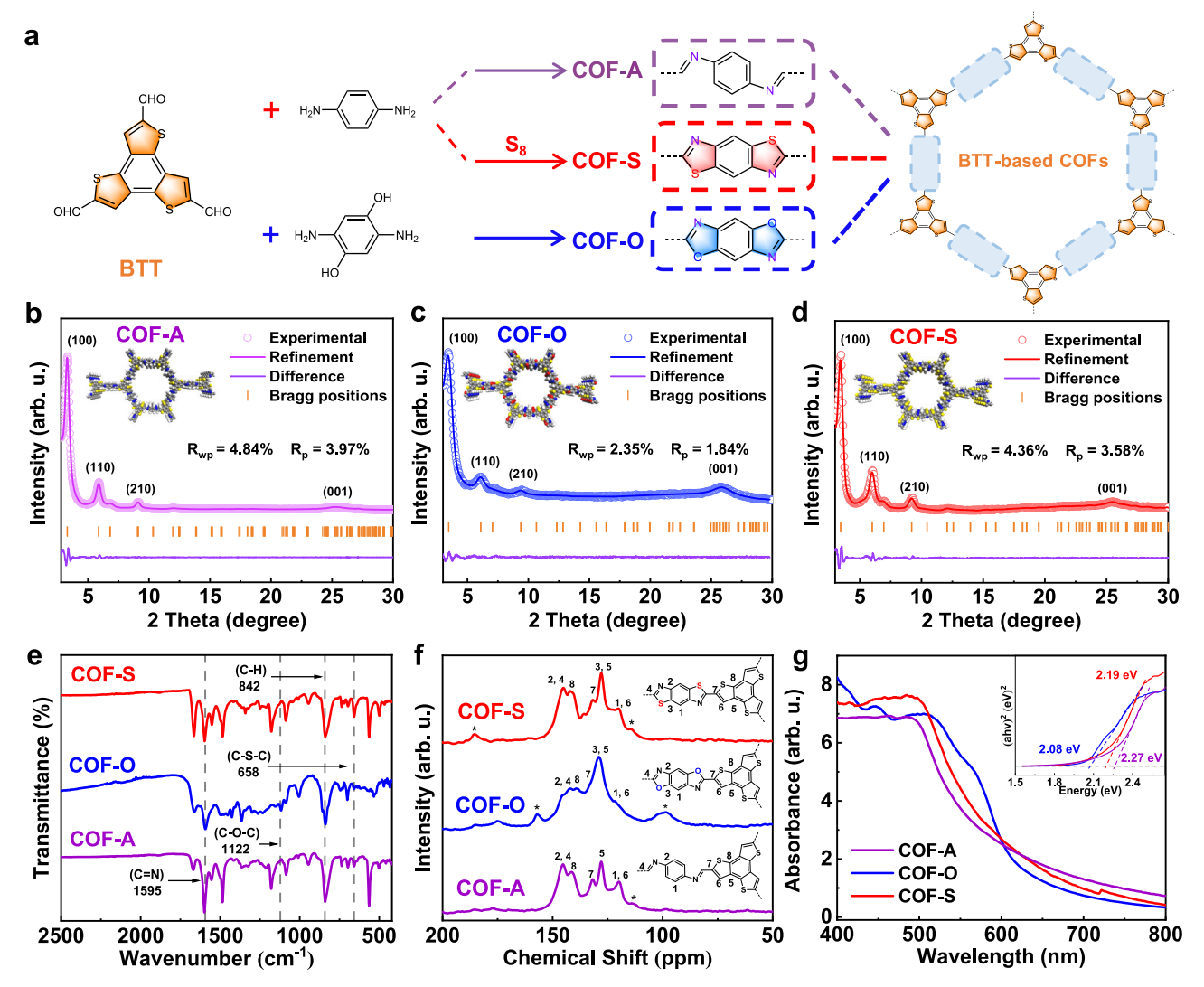


Fig. 1 | **Synthesis and structural characterizations.** Preparation scheme of COF-A, COF-O, and COF-S (**a**). Experimental and simulated PXRD patterns of COF-A (**b**), COF-O (**c**), and COF-S (**d**). FT-IR spectra (**e**) and ¹³C solid-state NMR spectra (**f**) of three COFs. UV-Vis DRS spectra of three COFs (**g**), the inset is the corresponding Tauc plot.

Results and discussion

Material characterizations

Via the condensation between benzo[1.2-b:3.4-b':5.6-b"]trithiophene-2,5,8-tricarbaldehyde (BTT, can achieve π -electron delocalization along the conjugated skeleton owing to its benzotrithiophene structure²²) and benzene-1,4-diamine, the imine-linked COFs (named as COF-A) are fabricated (Fig. 1a). The imine-linked COFs can be transformed into thiazole-linked COFs (named as COF-S) by directly adding sulfur (S₈) in the synthesized process of COF-A (Fig. 1a)²³. The oxazole-linked COFs (named as COF-O, as comparison rigid COFs) are also synthesized by the substitution of benzene-1,4-diamine with 2,5diaminobenzene-1,4-diol²⁴. The powder X-ray diffraction (PXRD) patterns of COF-A, COF-O, and COF-S reveal that all three COFs contain high crystalline structures owing to the existence of sharp diffraction peaks (Fig. 1b-d). Specifically, COF-A exhibits the diffraction peaks at 3.41°, 5.84°, 9.13°, and 25.51° (Fig. 1b). Similar peaks at 3.45°, 5.99°, 9.34°, and 25.79° are observed in the PXRD pattern of COF-O (Fig. 1c) and those at 3.43°, 5.95°, 9.28°, and 25.41° are present in the corresponding PXRD pattern of COF-S (Fig. 1d). These peaks can be assigned to (100), (110), (210), and (001) facets, respectively²⁵. The experimental PXRD pattern of all three COFs can be closely reproduced by Pawley refinement and fit well with the PXRD patterns simulated by the eclipse stacking (A-A stacking) model (Fig. 1b-d)23. The refined lattice parameters with low residual values (R_{wp} < 5% and R_p < 4%) for three COFs are given in Supplementary Tables 1-3.

The stretching vibrations at 842 and 1595 cm⁻¹ in the Fourier transform-infrared (FT-IR) spectra of three COFs correspond to the C -H and C=N bonds in the skeleton, respectively (Fig. 1e)²⁶. The presence of typical vibration of C-O-C at 1122 cm⁻¹ in COF-O indicates the successful formation of the oxazole linkages in COF-O. While the presence of strong stretch of C-S-C at 658 cm⁻¹ in COF-S shows that the thiazole linkages have been formed in COF-S27. The signals at ~120, ~128, ~132, and ~141 ppm in solid state ¹³C nuclear magnetic resonance (NMR) spectra for all three COFs can be assigned to the carbon atoms in the benzotrithiophene structure (Fig. 1f)²⁸. Moreover, the stronger carbon signal at ~128 ppm in ¹³C NMR spectra of both COF-O and COF-S relative to that of COF-A can be assigned to carbon atoms of benzoxazole and benzothiazole, respectively. This further confirms the successful conversion of imine linkage in COF-A to oxazole linkage in COF-O and thiazole linkage in COF-S, respectively. The X-ray photoelectron spectroscopy (XPS) survey spectra clearly indicate that all three COFs are composed of the elements of C, N, S, and O (Supplementary Fig. 1). Specifically, the high-resolution O 1s spectra of three COFs can be divided into two peaks at ~531.5 and ~533.1 eV (Supplementary Fig. 2a-c), which are ascribed to the O atoms in C=O bond (from the periphery of COFs) and C-O bond (from the -OH/H₂O absorbed on COFs), respectively²⁹. Comparing with COF-A and COF-S, the proportion of the C-O peak in COF-O significantly increases due to the presence of the extra oxazole linkages in COF-O, which further confirms the successful formation of the oxazole linkages in COF-O. The highresolution S 2p spectra of three COFs is deconvoluted into two peaks at ~163.8 and ~165.0 eV (Supplementary Fig. 2d-f), which are assigned to the S $2p_{3/2}$ and S $2p_{1/2}$, respectively⁴. All these characterization results confirm the successful formation of the as-designed structure in three COFs.

The Brunauer–Emmett–Teller (BET) specific surface areas of COFA, COF-O, and COF-S are 1800, 458, and 608 m² g⁻¹, respectively (Supplementary Fig. 3a–c). The decreased surface area of rigid COFs relative to the original ones can be ascribed to the blocking of pores in COFs by oligomers or linkers during the synthesis process^{30,31}. All three COFs have rod-like morphology with an average diameter of ~60 nm (Supplementary Fig. 4a–c). The high-resolution transmission electron microscopy (HR-TEM) images show that the lattice fringe of all three COFs can match well with their pore sizes, which confirms the high crystallinity of these COFs (Supplementary Fig. 4a–c insets)²⁷.

Comparing with COF-A, both COF-O and COF-S exhibit superior chemical stability under harsh conditions (in 1 mol L⁻¹ HCl or in 1 mol L⁻¹ NaOH solution for 12 h) (Supplementary Fig. 5). This indicates that linking COFs by rigid thiazole/oxazole linkages can enhance their chemical stability^{31,32}. Moreover, COF-S still contains excellent chemical stability even after being soaked either in 1 mol L⁻¹ HCl or in 1 mol L⁻¹ NaOH solution for 24 h, which suggests the potential stability of COF-S during its usage. The UV-vis diffuse reflectance spectroscopy (DRS) shows that all three COFs have a wide absorption band in the visiblelight region (Fig. 1g), indicating their strong visible-light harvesting properties. The corresponding bandgaps for COF-A, COF-O, and COF-S are calculated to be 2.27, 2.08, and 2.19 eV, respectively (Fig. 1g inset). All three COFs exhibit positive slopes in the Mott-Schottky plots (Supplementary Fig. 6a), which suggests that they are n-type semiconductors³³. Furthermore, the flat-band potentials (E_{fb}) of COF-A, COF-O, and COF-S are determined to be -0.46, -0.41, and -0.35 V vs. NHE, respectively. According to the XPS valence-band spectra (Supplementary Fig. 6b), the valence-band positions (E_{VB}) of COF-A, COF-O, and COF-S are estimated to be 1.68, 1.50, and 1.72 V vs. NHE, respectively, which suggests that h^+ photogenerated by three COFs has strong oxidation potential^{34,35}. The conduction band positions (E_{CR}) of three COFs are deduced to be -0.59, -0.58, and -0.47 V vs. NHE, respectively, which indicates that e photogenerated at these locations has a high reduction potential to produce $\cdot O_2^-$ ($O_2/\cdot O_2^-$, -0.33 V vs. NHE) (Supplementary Fig. 6c)⁴. Clearly, the photogenerated carriers in all three COFs have suitable redox potentials to produce reactive species for the elimination of micropollutants.

The electrostatic potential (ESP) analysis shows that the positive potential region of three COFs is mainly distributed on the benzotrithiophene structure, while the negative potential region is localized on the N atoms of imine/oxazole/thiazole linkage (Fig. 2a-c). This suggests that the local charge polarization in all three COFs causes the spatial separation of positive and negative charges³⁶. Moreover, the ESP area counts of three COFs follows the order of COF-S (2090) > COF-O (1977) > COF-A (580) (Supplementary Fig. 7). This demonstrates that linking COFs by rigid thiazole/oxazole linkages can improve π -conjugation and polarity for charge separation. Owing to the smallest differences of electronegativity between S and C atoms among three COFs as well as the presence of empty d orbital in thiazole linkages of COF-S $^{37\text{--}39}\!,$ the thiazole-linked COF-S has the greatest $\pi\text{--}$ conjugation and highest polarity for charge separation among all three COFs. The dipole moments of the repeating unit for three COFs are further calculated to be 2.12 (COF-A), 2.28 (COF-O), and 2.31 Debye (COF-S) (Supplementary Fig. 8), which is consistent with the trend of polarity for charge separation in three COFs. In addition, the S_m value (the overlap integral of hole-electron distribution) in the excited state of three COFs follows the order of COF-S (0.45 arb. u.) < COF-O (0.46 arb. u.) < COF-A (0.50 arb. u.) (Supplementary Fig. 8). This also confirms that linking COFs by rigid thiazole/oxazole linkages is favorable for π -conjugation and polarity for charge separation with best π conjugation and local charge separation property for COF-S¹⁷.

The transient photocurrent of all three COFs follows the order of COF-A (-3.1 μA cm $^{-2}$) < COF-O (-5.6 μA cm $^{-2}$) < COF-S (-7.9 μA cm $^{-2}$) (Fig. 2d), which demonstrates that linking COFs by rigid thiazole/oxazole linkages can improve the charge separation efficiency. The semicircle diameter in the high-frequency region of electrochemical impedance spectra (EIS) for all three COFs follows the order of COF-A > COF-O > COF-S (Fig. 2e). This further suggests that despite all three COFs have excellent electronic conductivity and supercapacitive characteristics, linking COFs by rigid thiazole/oxazole linkages yet can reduce the charge transfer resistance and enhance the conductivity of COFs 40 . Moreover, in two rigid COFs, COF-S has superior charge separation efficiency and lower internal charge transfer resistance relative to COF-O 41 . The photoluminescence (PL) intensity of COF-A is higher than two rigid COFs (with the lowest intensity for COF-S)

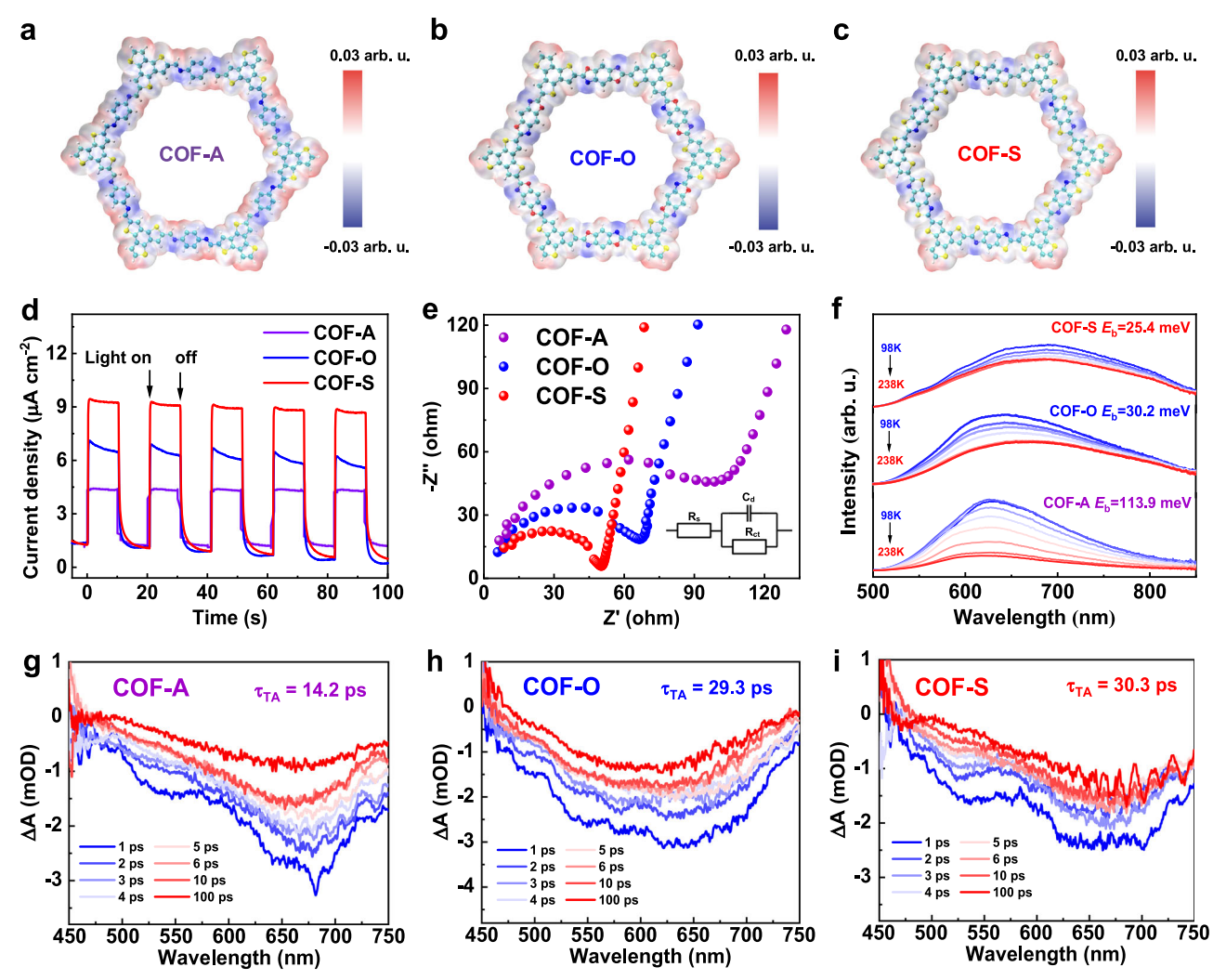


Fig. 2 | **Charge separation and transfer mechanism.** Electrostatic potential (ESP) of COF-A (**a**), COF-O (**b**), and COF-S (**c**). Photocurrent responses of three COFs (**d**). ElS measurement of three COFs (**e**), the inset is the corresponding impedance

fitting at high-frequency region. Temperature-dependent PL spectra of three COFs (\mathbf{f}). TA spectra of COF-A (\mathbf{g}), COF-O (\mathbf{h}), and COF-S (\mathbf{i}).

(Supplementary Fig. 9a), which indicates that linkage of COFs with rigid thiazole/oxazole linkages can suppress charge recombination. The average lifetimes (τ_{PL}) of PL decay curves are calculated to be 1.06, 0.76, and 0.38 ns for COF-A, COF-O, and COF-S, respectively (Supplementary Fig. 9b). The reduced delayed fluorescence lifetime suggests the more effective charge transport dynamics in COFs, which further demonstrates that linking COFs by rigid thiazole/oxazole linkages can promote nonradiative rate and charge transfer efficiency with the best performance for thiazole-linked COF-S⁴². These results clearly exhibit that the charge separation efficiency of all three COFs follows the order of COF-A < COF-O < COF-S, which is consistent with the trend of π -conjugation and polarity in three COFs.

To further evaluate the impact of linkage with different π-conjugation and polarity in COFs on the exciton (e^-h^+ pair) dissociation behaviors, the exciton binding energy (E_b) was estimated from the temperature-dependent PL measurements⁴³. The E_b of all three COFs is in the order of COF-A (113.9 meV) > COF-O (30.2 meV) > COF-S (25.4 meV) (Fig. 2f). This suggests that thiazole/oxazole linkage is favorable for exciton dissociation with the highest dissociation efficiency for COF-S with thiazole linkage. The broad and negative absorbance changes in the femtosecond time-resolved transient absorption (fs-TA) spectroscopy of three COFs (Fig. 2g-i) can be attributed to the photoinduced excited-state absorption on ultrafast time scales⁴⁴. The lifetime (τ_{TA}) of photoinduced exciton follows the

order of COF-A (14.2 ps) < COF-O (29.3 ps) < COF-S (30.3 ps) (Supplementary Fig. 10), which suggests that thiazole/oxazole linkage can improve the lifetime of excited charges in COFs and is beneficial for the dissociation of excitons⁴⁵. Moreover, comparing with COF-O with oxazole linkage, COF-S with thiazole linkage has longer-lived excited charges⁴⁶. Clearly, the excitons in both thiazole-linked COF-S and oxazole-linked COF-O can more efficiently dissociate to free charges than COF-A without rigid linkage. Meanwhile, in two rigid COFs, the excitons dissociation in thiazole-linked COF-S is more effective relative to oxazole-linked COF-O. The charge separation efficiency of three COFs obtained from TA decay kinetics thus also follows the order of COF-A < COF-O < COF-S, which is consistent with the result acquired from PL decay curves⁴⁷. This further indicates that COF-S, with the best π -conjugation and local charge polarization, can generate more free charges and the subsequent reactive species for the elimination of micropollutants than COF-A and COF-O.

Photocatalytic degradation performance

The degradation performance of three COFs towards a model emerging organic pollutant (paracetamol, also known as acetyl-para-aminophenol (APAP)) under visible-light irradiation was investigated (Fig. 3a and Supplementary Fig. 11). Without the addition of any photocatalyst, 5 mg L⁻¹ paracetamol can hardly be removed under visible-light irradiation. P25 and g-C₃N₄, two typical photocatalysts, have

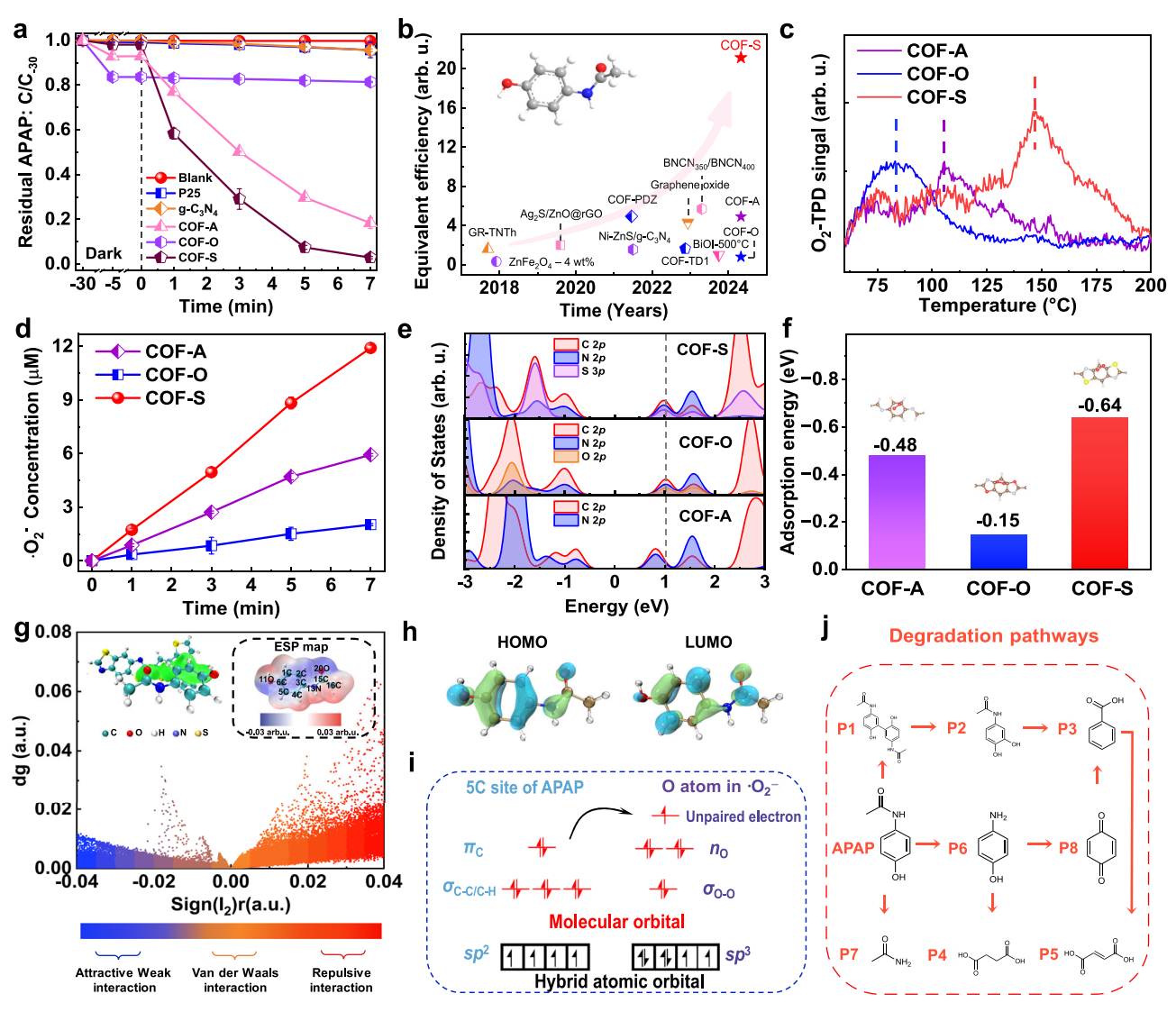


Fig. 3 | **Photocatalytic performance and degradation pathways.** Photocatalytic performance for paracetamol degradation by three COFs (a). Comparison of photocatalytic degradation performance towards paracetamol by different photocatalysts (b). O_2 -TPD curves of three COFs (c). O_2 -yield of three COFs (d). PDOS of three COFs based on benzene and imine/azole linkage (e). Adsorption energy of O_2 on three COFs (f). Non-covalent interactions between COF-S and paracetamol based on IGMH where the spheres colored silver, red, blue, yellow, and white

represent C, O, N, S, and H atoms, respectively (**g**), the inset is the surface electrostatic potential of paracetamol. HOMO and LUMO distribution of paracetamol (**h**). Electron transfer mechanism for paracetamol by $\cdot O_2^-$ on 5 C site at the molecular orbital level (**i**). Photocatalytic degradation pathways of paracetamol (**j**). Error bars represent the standard deviation and are calculated on the basis of two independent experiments.

negligible adsorption capability toward paracetamol, while COF-A, COF-O, and COF-S can adsorb 7.1, 16.4, and 1.9% of paracetamol after 30 min adsorption process, respectively. 4.3 and 4.4% of paracetamol can be removed by P25 and g-C₃N₄ in 7 min under visible-light irradiation, respectively. Although increasing reaction duration can increase paracetamol removal efficiencies by these two typical photocatalysts, only 48.0 and 55.7% of paracetamol yet are removed by P25 and g-C₃N₄ even after 180 min reaction duration under visible-light irradiation (Supplementary Fig. 12a). Comparing with both P25 and g-C₃N₄, COF-A has better paracetamol photocatalytic performance with 81.7% removal efficiency within 7 min reaction duration (Fig. 3a) and 98.2% removal efficiency after 30 min reaction under visible-light irradiation (Supplementary Fig. 12a).

Interestingly, even within 7 min reaction duration, 98.7% of paracetamol can be removed by COF-S under visible-light irradiation, which indicates that linking COFs by rigid thiazole can greatly improve the paracetamol removal performance. However, only 18.6% paracetamol is removed by COF-O in the first 7 min reaction

duration (1.8% paracetamol is photodegraded). The paracetamol removal efficiency by COF-O reaches 95.9% after 180 min reaction duration under visible-light irradiation (Supplementary Fig. 12a). This indicates although the paracetamol removal performance of COF-O is lower than COF-A and COF-S, which yet is still better than those of two typical photocatalysts (P25 and g-C₃N₄). The photocatalytic removal performance toward another emerging organic contaminant (tetracycline, TC) by different photocatalysts also follows the order of COF-S > COF-A > COF-O > typical photocatalysts (P25 and g-C₃N₄) (Supplementary Fig. 12b). Clearly, three COFs have better photocatalytic performance towards typical emerging organic contaminants than both P25 and g-C₃N₄. Among three fabricated COFs, COF-S contains the best photocatalytic removal performance towards typical emerging organic contaminants. Moreover, COF-S also shows superior photocatalytic removal capability towards model emerging organic contaminant (paracetamol) than other reported photocatalysts (Fig. 3b and Supplementary Table 4).

Photocatalytic mechanisms

To reveal the mechanisms driving the different photocatalytic performances of three COFs toward typical emerging organic contaminants, scavenger experiments and electron-spin resonance (ESR) spectra were conducted. The removal performance by COF-S is negligibly impacted in the presence of IPA (as a scavenger for ·OH) or D₂O (for improving the lifetime of ¹O₂)⁴⁸ (Supplementary Fig. 13). Accordingly, both DMPO-OH (Supplementary Fig. 14a) and TEMP-1O2 (Supplementary Fig. 14b) signals of COF-S reaction system are absent under visible-light irradiation. These results confirm the negligible contribution of both ·OH radicals and ¹O₂ to paracetamol removal by COF-S. When EDTA-2Na (scavenger for photogenerated h^+) is added into the reaction system, the paracetamol degradation performance of COF-S is slightly inhibited (Supplementary Fig. 13), which indicates that photogenerated h^+ has some contributions to the paracetamol degradation. Remarkably, only 2.8% paracetamol can be degraded within 7 min after the addition of p-BQ (scavenger for $\cdot O_2^-$ radical) into the photocatalytic system, which suggests that $\cdot O_2^-$ radicals play important roles in the degradation of paracetamol by COF-S. The increased ESR signal of DMPO-O₂ with increasing irradiation duration under visible-light irradiation confirms the generation of $\cdot O_2^-$ radicals in the reaction system (Supplementary Fig. 14c). Note that TEMPO signals are present in reaction system under dark conditions, while the corresponding signal intensity is decreased under visible-light irradiation (Supplementary Fig. 15a). Moreover, the signal intensity of TEMP (the reduction product of TEMPO) increases with increasing irradiation duration, which is consistent with the decreased signal intensity of TEMPO with increasing irradiation duration in LC-MS analysis (Supplementary Fig. 15b, c). This suggests the presence of a reaction between TEMPO and photogenerated e^- (to form spin-free TEMP) in the photocatalytic system (Supplementary Fig. 15c inset). Clearly, in the reaction system, the dissolved molecular oxygen can be captured by photogenerated e^- to form $\cdot O_2^-$ radicals under light irradiation for the following paracetamol degradation⁴⁹. The above results show that both the photogenerated h^+ and $\cdot O_2^-$ radicals (with a more significant effect) play important roles during the degradation process of paracetamol by COF-S. Since negligible paracetamol is removed by COF-S under dark conditions without irradiation, the paracetamol degradation achieved under visible-light irradiation thus is unlikely to occur within the pores or the interlayer of COF-S. Instead, paracetamol degradation resulted from the attack by free radicals (·O₂⁻) mainly occurs in the bulk solution, while that by h^+ locates on the surface of COF-S^{50,51}. The scavenger experiments for COF-A (Supplementary Fig. 16) and COF-O (Supplementary Fig. 17) also show that both photogenerated h^+ and $\cdot O_2^-$ radicals have contribution to paracetamol degradation in reaction systems of both COF-A and COF-O.

The relative contribution of h^+ to paracetamol degradation by COF-A, COF-O, and COF-S is calculated to be 22.0, 39.3, and 18.7%, respectively, while that of $\cdot O_2^-$ radicals to paracetamol degradation by COF-A, COF-O, and COF-S is 78.0, 60.7, and 81.3%, respectively. The relatively large contributions of $\cdot O_2^-$ radicals (formed by reaction between dissolved molecular oxygen and photogenerated e^{-}) to paracetamol degradation in three COFs reaction systems imply that the activation of dissolved oxygen plays an important role in the reaction process. The significant decreases of paracetamol degradation efficiency obtained in reaction systems of all three COFs with purging N₂ to remove dissolved oxygen confirm the vital role of O₂ during paracetamol degradation process (Supplementary Fig. 18). The O₂-TPD experiments show that the adsorption capacity of three COFs towards O₂ is in the order of COF-S > COF-A > COF-O (Fig. 3c), which confirms that COF-S can relatively easier adsorb O2 than COF-A and COF- 0^{52} . NBT probe experiments demonstrate that the amount of $\cdot 0_2^{-1}$ radicals generated in the COF-S system within 7 min of visible-light irradiation is the largest (11.9 μmol L⁻¹), which is followed by COF-A (5.9 µmol L⁻¹) and then by COF-O (2.0 µmol L⁻¹) (Fig. 3d). This result indicates that comparing with COF-A and COF-O, the enhanced $\rm O_2$ activation on COF-S is one of the important reasons driving to the excellent degradation performance of COF-S.

The O₂ activation process by three COFs was further revealed by density functional theory (DFT) calculation. The partial density of states (PDOS) shows that the conduction band bottom in three COFs located on the phenyl and azole ring consists of C 2p and N 2p states (with extra O 2p states for COF-O and S 3p states for COF-S) (Fig. 3e). Comparing with COF-A, the C 2p states in COF-O and COF-S move toward a more positive region. Moreover, C 2p states of COF-S locate between those of COF-A and COF-O. The more positive C 2p states can easily induce the formation of unstable chemical bond between COFs and O₂ molecules, while the more negative C 2p states likely causes the formation of inert chemical bond between COFs and O2 molecules (unfavorable for the O₂ activation either)⁵³. Therefore, comparing with COF-A and COF-O, a moderate location of C 2p in COF-S can effectively modulate the activities of neighboring benzene units to boost the oxygen activation capacity³⁹. The adsorption energy of O₂ on COF-A, COF-O, and COF-S is calculated to be -0.48, -0.15, and -0.64 eV, respectively (Fig. 3f). This confirms that O₂ is prone to be adsorbed onto thiazole-linked COF-S, which follows by imine-linked COF-A and then oxazole-linked COF-O. Moreover, similar to those of COF-A (0.69 eV) and COF-O (0.68 eV), the desorption energy barrier of $\cdot O_2^-$ on COF-S (0.65 eV) is also less than 0.75 eV (below this value, the energy barrier can be surmountable at room temperature) (Supplementary Fig. 19)⁵⁴. This implies that $\cdot O_2^-$ radicals generated on the surfaces of COF-S, as well as those COF-A and COF-O, can easily diffuse into solution to attack paracetamol and leads to its degradation. Clearly, in addition to the excellent charge separation efficiency, thiazole-linked COF-S also has superior O₂ adsorption property and the extraordinary ·O₂ radicals generation as well as desorption capabilities, resulting in the efficient paracetamol degradation performance. In contrast, owing to the lowest O_2 adsorption capability and the weakest subsequent O_2 radicals generation performance, COF-O exhibits low paracetamol degradation capability regardless of its high charge separation performance and $\cdot O_2^-$ radicals desorption capability.

COF-S exhibits overall negative zeta potentials at the experimental pH condition (pH 7) (Supplementary Fig. 20), while paracetamol contained regions of positive potentials located on 1C, 4C, 16C, and 13N atoms (Fig. 3g inset). The paracetamol molecular thus can be first pulled to surfaces of COF-S via attractive electrostatic force and then by van der Waals interaction (Fig. 3g)55. The HOMO and LUMO distribution of paracetamol, mainly located on the phenyl ring and amine group can be easily attacked by the reactive species ($\cdot O_2^-$ radicals and h^+) (Fig. 3h). The proton abstraction and C-N bond cleavage resulted from h^+ and $\cdot O_2^-$ radicals attack contribute to the degradation of paracetamol by COF-S (Supplementary Tables 5, 6)⁵⁶. Firstly, the most reactive 5 C atom ($f^0 = 0.083$) of paracetamol is sp^2 -hybridization, including three σ orbitals and one π orbital (Fig. 3i)⁵⁷. The electron with higher reactivity in the 5C atom tends to be captured by $\cdot O_2^-$ radical to yield byproduct P1, which can be further attacked to form byproduct P2 (Fig. 3i, j). Byproduct P2 can be oxidized into byproduct P3 and further oxidized to form a ring-opening product P4 and P558. On the other hand, the direct cleavage of the C-N bond for 13N ($f^0 = 0.042$) in paracetamol can also generate product P6, or form another primary byproduct P7⁵⁶. The byproduct P6 can also be oxidized by \cdot O₂ radicals to convert into byproducts P4 and P5. Moreover, the byproduct P6 contained an amino group that can be readily attacked by O_2 radicals to generate byproduct P8 and further oxidized into byproduct P3⁵⁸. The estimated mutagenicity toxicities of the byproducts P3-P8 generated during the paracetamol degradation process are all mutagenicity negative (with lower mutagenicity for final product P4 and P7 relative to paracetamol) (Supplementary Fig. 21), suggesting the low ecological risks of photocatalytic paracetamol degradation by COF-S⁵⁹. The proposed degradation mechanisms of paracetamol by COF-S are



Fig. 4 | **Photocatalytic mechanism.** Mechanism diagram of photocatalytic degradation towards paracetamol by three COFs. In the models, the spheres colored silver, red/purple, blue, yellow, and white represent C, O, N, S, and H atoms,

respectively, while the spheres colored light blue and light purple represent the photogenerated electrons and holes, respectively.

presented in Fig. 4. Thiazole-linked COF-S with superior charge separation efficiency, and O_2 adsorption property can generate more O_2 radicals as well as h^+ under light irradiation, which subsequently attack paracetamol and lead to its degradation.

Universality, reusability, and application feasibility

Under different water chemistry conditions at a wide initial solution pH range (from 3 to 11) (Fig. 5a), with a broad ionic strength range (from 0 to 50 mM NaCl) (Fig. 5b), with coexisting various types of anions (Cl-, CO_3^{2-} , NO_3^{-} , and SO_4^{2-}) (Fig. 5c) and with copresence of natural organic matter (NOM, 0 to 5 mg L⁻¹ humic acid) (Fig. 5d), COF-S can still effectively degrade paracetamol under visible-light irradiation. Even in four real water samples including tap water (TW), lake water (LW), river water (RW), and seawater (SW), more than 98% of paracetamol can be degraded within 30 min (Fig. 5e). These results confirm the potential application of COF-S for the elimination of paracetamol under complex water matrix and in actual water samples. In addition to paracetamol and tetracycline, COF-S can also effectively eliminate other organic contaminants such as bisphenol A (BPA), diclofenac (DCF), ciprofloxacin (CIP), sulfadiazine (SDZ) and naproxen (NPX) under visible-light irradiation (Fig. 5f). Moreover, COF-S can also efficiently inactivate antibiotic-resistant bacteria (ARB, Escherichia coli, E. coli S-17) containing gentamycin resistance genes (gmrA) (Supplementary Fig. 22a) and harmful algae Microcystis aeruginosa (M. aeruginosa) (Supplementary Fig. 22b). These results demonstrate that COF-S not only contains excellent emerging organic contaminant photodegradation capability, but also has efficient microbe inactivation property, confirming the universal water decontamination capability of COF-S.

Comparing with that of fresh ones, XRD patterns, FT-IR spectra, SEM morphology, and BET surface areas of COF-S after five reused experiments do not change dramatically, suggesting the relative photo-stability of COF-S under visible-light irradiation

(Supplementary Fig. 23a-d). Moreover, COF-S not only exhibits more excellent chemical stability under harsh conditions (either in 1 mol L⁻¹ HCl or 1 mol L⁻¹ NaOH solution for 24 h) than COF-A (Supplementary Fig. 5), but also maintains higher stability (Supplementary Fig. 23) and superior paracetamol degradation efficiency during the overall five reused experiments compared with COF-A (Fig. 5g). To ease its recovery and reuse, COF-S can be immobilized onto a continuous-flow reactor (Fig. 5h and Supplementary Fig. 24) and an enlarged reactor (Fig. 5i inset). Over 92% of paracetamol can be consecutively degraded by COF-S in the continuous-flow reactor system throughout the whole 20 h reaction process (Fig. 5h). The excellent photocatalytic paracetamol degradation performance during the whole reaction process indicates that the feasibility of COF-S for the successive degradation of paracetamol. Despite the sunlight intensity fluctuation (Supplementary Fig. 25), efficient paracetamol degradation performance in five consecutive reused experiments in an enlarged reactor (50 cm × 30 cm × 5 cm) of 2L working volume with immobilized COF-S (200 mg) under natural sunlight irradiation is achieved (Fig. 5i). This demonstrates the excellent stability and high photocatalytic efficiency of COF-S towards typical emerging organic pollutant under natural sunlight irradiation. The above results clearly show that COF-S has great potentials for the practical applications to eliminate micropollutants in water through an energy-saving and cost-effective way.

In summary, we propose a simple strategy for the design of rigid COFs by converting the reversible imine linkages into rigid thiazole linkages for the elimination of micropollutants in water. We find that linking COFs by rigid thiazole rings significantly adjusts the π -conjugation and local charge polarization of the skeleton to facilitate the exciton dissociation of COFs. The increased robustness of skeletons in rigid linkages also improves the structure stability of COFs. More importantly, the thiazole linkages in COF-S with

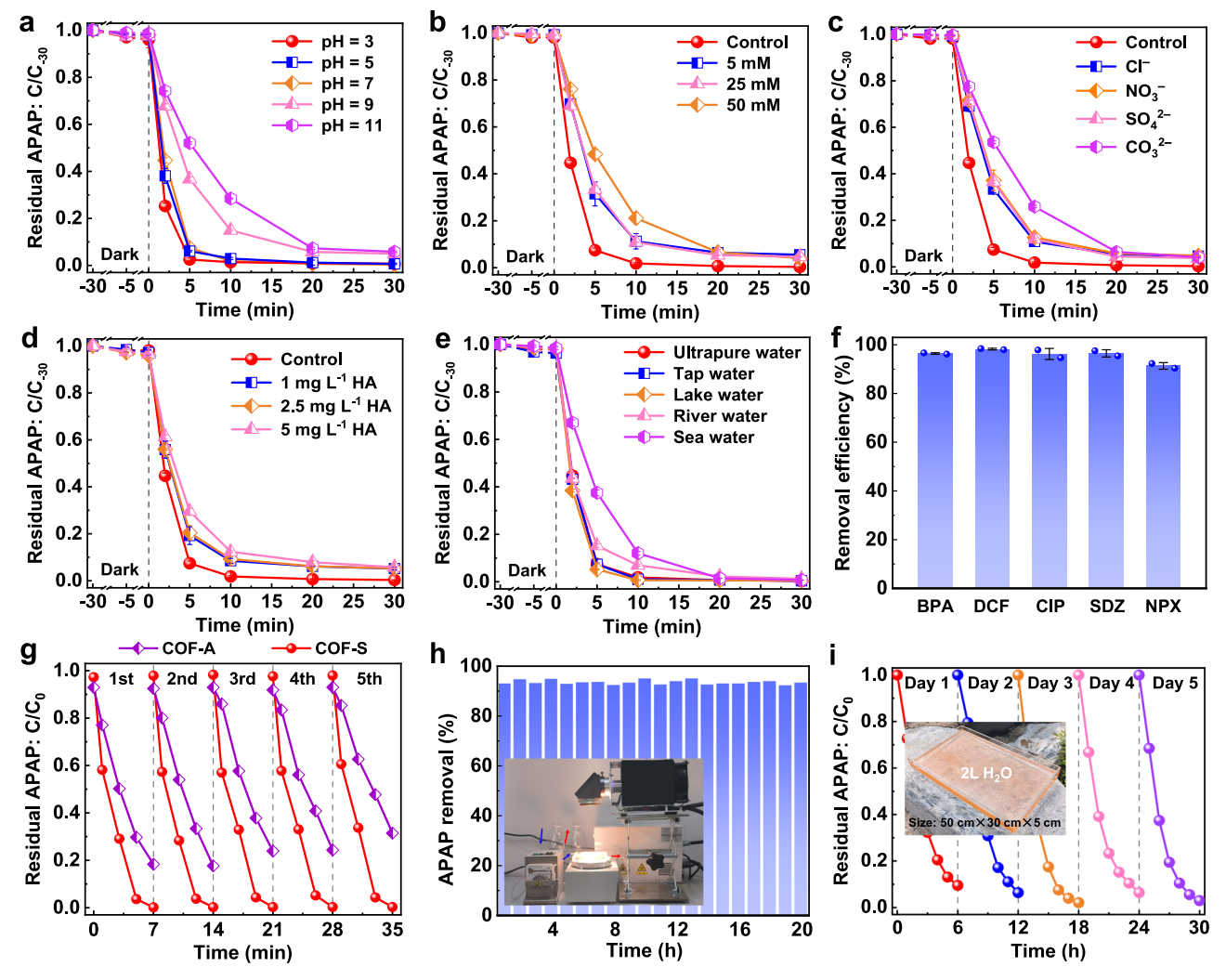


Fig. 5 | **Feasibility investigation for practical applications.** Photocatalytic performance for paracetamol degradation by COF-S at different initial solution pH (a), with different ionic strengths (b), coexisting anions (c), coexisting of humic acid (d), and in different real water samples (e). Photocatalytic degradation performance of COF-S towards five other emerging contaminants (f). Reusability of COF-A and COF-S towards paracetamol degradation under visible-light irradiation (g).

Degradation performance of paracetamol by immobilized COF-S in a continuous-flow reactor under visible-light irradiation for 20 h (h) and in an enlarged reactor of 2 L under natural sunlight irradiation in 5 days (i), the insets are the corresponding digital image of the photocatalytic degradation experiment using different reactors. Error bars represent the standard deviation and are calculated on the basis of two independent experiments.

optimal C 2p states effectively increase the activities of neighboring benzene units to directly modulate the O2-adsorption energy barrier, resulting in highly efficient O2 activation. The efficient paracetamol degradation by COF-S is achieved in a complex water matrix and in four actual waters. The high degradation efficiencies of the other six emerging contaminants, together with the inactivation of ARB and harmful algae confirms the universal pollutant elimination capability of COF-S. Besides, COF-S can be immobilized in continuous-flow reactor and in enlarged reactor under natural sunlight irradiation to efficiently eliminate paracetamol, which provides an energy-saving and cost-effective way for the practical application of COF-S to remove micropollutants in water. Overall, this work not only gives insights into the design of rigid COFs by thiazole linkage for the efficient photocatalytic removal of micropollutants from water, but also paves the way for the practical application of COFs photocatalysts in water decontamination.

Methods

Synthesis of COF-A

Imine-linked COF-A was synthesized based on the Schiff-base reaction via a solvothermal method. Specifically, a mixture of BTT

(132.2 mg, 0.4 mmol), benzene-1,4-diamine (64.9 mg, 0.6 mmol), mesitylene (6 mL), 1,4-dioxane (4 mL), and acetic acid (HAc, 1 mL, 6 M) was added into a 20 mL Teflon lining and then treated by ultrasonication for 20 min, which was then sealed in an autoclave and put into an oven and heated at 120 °C for 3 days. The precipitate was isolated by filtration and washed with acetone three times. After drying at 60 °C under air for 12 h, the final product was obtained (163 mg, 83% yield).

Synthesis of COF-S

Thiazole-linked COF-S was synthesized by a facile one-pot synthesis strategy 24 . Specifically, a mixture of BTT (132.2 mg, 0.4 mmol), benzene-1,4-diamine (64.9 mg, 0.6 mmol), sulfur (S $_8$, 115.2 mg, 3.6 mmol), dimethyl sulfoxide (0.5 mL), ortho-dichlorobenzene (4.5 mL), ethanol (5.0 mL) and HAc (0.8 mL, 6 M) was added into a 20 mL Teflon lining and then treated by ultrasonication for 20 min, which was then sealed in an autoclave and put into an oven and heated at 120 °C for 3 days. The precipitate was isolated by filtration and washed with acetone three times. After drying at 60 °C under air for 12 h, the final product was obtained (152 mg, 49% yield).

Synthesis of COF-O

Oxazole-linked COF-O was synthesized by a facile one-pot synthesis strategy²³. Specifically, a mixture of BTT (132.2 mg, 0.4 mmol), 2,5-diaminobenzene-1,4-diol (127.8 mg, 0.6 mmol), *N*-methyl-2-pyrrolidone (NMP, 5 mL), and mesitylene (5 mL), was added into a 20 mL Teflon lining and then treated by ultrasonication for 20 min, which was then sealed in an autoclave and put into an oven and heated at 185°C for 5 days. The precipitate was isolated by filtration and washed with acetone three times. After drying at 60 °C under air for 12 h, the final product was obtained (192 mg, 74% yield).

Catalyst characterization

PXRD (X-Pert3, PANalytical, Netherlands), ¹³C NMR (AVANCE III, Bruker, Switzerland), FT-IR (Nicolet is50, Thermo Fisher, USA), XPS (Axis Ultra, Kratos, UK), SEM (S-4800, HITACHI, Japan), and TEM (Tecnai F30, FEI, USA) were employed to reveal the chemical and structural information of three COFs. UV-vis DRS (UV3600PLUS, Shimadzu, Japan), steady state PL spectra, time-resolved PL decay curve, temperature-dependent PL spectra (FLS980, Edinburgh, UK), TA spectrometer (Helios, Ultrafast System, USA), ESR analysis (Bruker EMX, Bruker, Switzerland), and EIS (CHI760E, Chenhua, China) were performed to investigate the mechanisms of the fabricated COFs.

Photocatalytic experiments

The photocatalytic degradation performance of micropollutants by all three COFs was first examined in a double-walled reactor with 60 mL of 5 mg L⁻¹ paracetamol solution and 12 mg of COFs (Supplementary Fig. 26). The reaction suspension was irradiated by using a 300 W Xenon lamp ($\lambda > 420 \text{ nm}$, $100 \pm 1 \text{ mW cm}^{-2}$). The temperature was fixed at 25.0 ± 0.2 °C by circulating water system during the photocatalytic experiments. The reaction suspension was extracted and filtered for micropollutant measurement at specific time intervals. The effects of different water matrix, including initial solution pH, ionic strengths, coexisting anions, and natural organic matter on photocatalytic degradation of paracetamol by COF-S are systematically examined. The degradation capability of COF-S in real water samples, including tap, river, lake, and sea water are also explored. The repeat photocatalytic performance towards paracetamol degradation in the enlarged reactor outdoors with natural sunlight irradiation were performed on 5 sunny days (November 2023) in the campus of Peking University (116°E, 40°N), China.

Reporting summary

Further information on research design is available in the Nature Portfolio Reporting Summary linked to this article.

Data availability

The data generated in this study are provided in the Supplementary Information and Source Data file. Source data are provided with this paper.

References

- Wang, J., Zhi, D., Zhou, H., He, X. & Zhang, D. Evaluating tetracycline degradation pathway and intermediate toxicity during the electrochemical oxidation over a Ti/Ti₄O₇ anode. Water Res. 137, 324–334 (2018).
- Wu, T. et al. Solar-driven efficient heterogeneous subminute water disinfection nanosystem assembled with fingerprint MoS₂. Nat. Water 1, 462–470 (2023).
- Zhan, H., Zhou, R., Wang, P. & Zhou, Q. Selective hydroxyl generation for efficient pollutant degradation by electronic structure modulation at Fe sites. *Proc. Natl Acad. Sci. USA* 120, e2305378120 (2023).

- Qin, C. et al. Twistedly hydrophobic basis with suitable aromatic metrics in covalent organic networks govern micropollutant decontamination. *Nat. Commun.* 14, 6740 (2023).
- Feng, S. et al. Regulation of the tertiary N site by edge activation with an optimized evolution path of the hydroxyl radical for photocatalytic oxidation. ACS Catal. 13, 8708–8719 (2023).
- Khatri, J., Nidheesh, P. V., Anantha Singh, T. S. & Suresh Kumar, M. Advanced oxidation processes based on zero-valent aluminium for treating textile wastewater. *Chem. Eng. J.* 348, 67–73 (2018).
- Yan, Y. et al. Van der Waals heterojunction between a bottom-up grown doped graphene quantum dot and graphene for photoelectrochemical water splitting. ACS Nano 14, 1185–1195 (2020).
- Dai, B. et al. Construction of infrared-light-responsive photoinduced carriers driver for enhanced photocatalytic hydrogen evolution. Adv. Mater. 32, 1906361 (2020).
- Zhao, Y. et al. Reduced graphene oxide supported ZnO/CdS heterojunction enhances photocatalytic removal efficiency of hexavalent chromium from aqueous solution. Chemosphere 286, 131738 (2022).
- 10. Deng, Y. et al. Engineering the photocatalytic behaviors of g/C_3N_4 -based metal-free materials for degradation of a representative antibiotic. *Adv. Funct. Mater.* **30**, 2002353 (2020).
- Zhu, C. et al. Insights into the crucial role of electron and spin structures in heteroatom-doped covalent triazine frameworks for removing organic micropollutants. *Environ. Sci. Technol.* 56, 6699–6709 (2022).
- Liu, W. et al. Visible-light-driven photocatalytic degradation of diclofenac by carbon quantum dots modified porous g-C₃N₄: Mechanisms, degradation pathway and DFT calculation. Water Res. 151, 8–19 (2019).
- Wang, Q.-Y. et al. Aminal-linked porphyrinic covalent organic framework for rapid photocatalytic decontamination of mustard-gas simulant. Angew. Chem. Int. Ed. 61, e202207130 (2022).
- Zhou, Z.-B. et al. Toward azo-linked covalent organic frameworks by developing linkage chemistry via linker exchange. *Nat. Commun.* 13, 2180 (2022).
- Cheng, J. et al. Fully conjugated 2D sp² carbon-linked covalent organic frameworks for photocatalytic overall water splitting. Adv. Mater. 36, 2305313 (2024).
- Karak, S. et al. A covalent organic framework for cooperative water oxidation. J. Am. Chem. Soc. 144, 17661–17670 (2022).
- 17. Li, Y. et al. In situ photodeposition of platinum clusters on a covalent organic framework for photocatalytic hydrogen production. *Nat. Commun.* **13**, 1355 (2022).
- Chen, J., Yuan, D. & Wang, Y. Covalent organic frameworks based heterostructure in solar-to-fuel conversion. Adv. Funct. Mater. 33, 2304071 (2023).
- Zhang, M. et al. Semiconductor/covalent-organic-framework Z-scheme heterojunctions for artificial photosynthesis. *Angew. Chem. Int. Ed.* 59, 6500–6506 (2020).
- Liu, C. et al. Intrinsic activity of metal centers in metal-nitrogen-carbon single-atom catalysts for hydrogen peroxide synthesis. J. Am. Chem. Soc. 142, 21861–21871 (2020).
- Chang, J.-N. et al. Oxidation-reduction molecular junction covalent organic frameworks for full reaction photosynthesis of H₂O₂.
 Angew. Chem. Int. Ed. 62, e202218868 (2023).
- 22. Nicolas, Y. et al. Planarized star-shaped oligothiophenes with enhanced π-electron delocalization. *Org. Lett.* **6**, 273–276 (2004).
- Wei, P.-F. et al. Benzoxazole-linked ultrastable covalent organic frameworks for photocatalysis. J. Am. Chem. Soc. 140, 4623–4631 (2018).
- Paul, R. et al. Benzothiazole-linked metal-free covalent organic framework nanostructures for visible-light-driven photocatalytic conversion of phenylboronic acids to phenols. ACS Appl. Nano Mater. 4, 11732–11742 (2021).

- Wu, C.-J. et al. Natural sunlight photocatalytic synthesis of benzoxazole-bridged covalent organic framework for photocatalysis. J. Am. Chem. Soc. 144, 18750–18755 (2022).
- Liu, M. et al. Benzotrithiophene-based covalent organic frameworks as efficient catalysts for artificial photosynthesis of H₂O₂ in pure water. Chem. Eng. J. 482, 148922 (2024).
- Cui, W.-R. et al. Low band gap benzoxazole-linked covalent organic frameworks for photo-enhanced targeted uranium recovery. Small 17, 2006882 (2021).
- Jeon, J.-P. et al. Benzotrithiophene-based covalent organic framework photocatalysts with controlled conjugation of building blocks for charge stabilization. *Angew. Chem. Int. Ed.* 62, e202217416 (2023).
- Cao, Y. et al. Lithiation of covalent organic framework nanosheets facilitating lithium-ion transport in lithium-sulfur batteries. *Energy Storage Mater.* 29, 207–215 (2020).
- Liu, H. et al. Post-cyclization of a bisimine-linked covalent organic framework to enhance the performance of visible-light photocatalytic hydrogen evolution. *Polym. Chem.* 14, 1323–1329 (2023).
- Waller, P. J., AlFaraj, Y. S., Diercks, C. S., Jarenwattananon, N. N. & Yaghi, O. M. Conversion of imine to oxazole and thiazole linkages in covalent organic frameworks. *J. Am. Chem.* Soc. **140**, 9099–9103 (2018).
- 32. Miller, K. A. et al. High-strength, microporous, two-dimensional polymer thin films with rigid benzoxazole linkage. ACS Appl. Mater. Interfaces 14, 1861–1873 (2022).
- 33. Tan, H. et al. Photocatalysis of water into hydrogen peroxide over an atomic Ga- N_5 site. *Nat. Synth.* **2**, 557–563 (2023).
- Qin, C. et al. Dual donor-acceptor covalent organic frameworks for hydrogen peroxide photosynthesis. Nat. Commun. 14, 5238 (2023).
- Shen, R. et al. Realizing photocatalytic overall water splitting by modulating the thickness-induced reaction energy barrier of fluorenone-based covalent organic frameworks. Adv. Mater. 35, 2305397 (2023).
- Ben, H. et al. Local spatial polarization induced efficient charge separation of squaraine-linked COF for enhanced photocatalytic performance. Adv. Funct. Mater. 32, 2104519 (2022).
- 37. Tian, Y. et al. Synergy effect of porphyrin units and alkynyl π bridges tunes the memory behavior and threshold voltage of hyperbranched polyimides. *J. Phys. Chem. C.* **124**, 2872–2878 (2020).
- Zhao, M. et al. Studies of third-order optical nonlinearities of model compounds containing benzothiazole, benzimidazole and benzoxazole units. Chem. Mater. 2, 670–678 (1990).
- Mou, Y. et al. Linkage microenvironment of azoles-related covalent organic frameworks precisely regulates photocatalytic generation of hydrogen peroxide. *Angew. Chem. Int. Ed.* 62, e202309480 (2023).
- Yang, Y. et al. Grotthuss proton-conductive covalent organic frameworks for efficient proton pseudocapacitors. *Angew. Chem. Int. Ed.* 60, 21838–21845 (2021).
- Lu, M. et al. Rational design of crystalline covalent organic frameworks for efficient CO₂ photoreduction with H₂O. Angew. Chem. Int. Ed. 58, 12392–12397 (2019).
- 42. Yue, J.-Y. et al. Thiophene-containing covalent organic frameworks for overall photocatalytic H_2O_2 synthesis in water and seawater. Angew. Chem. Int. Ed. **62**, e202309624 (2023).
- Yan, H. et al. Spontaneous exciton dissociation in organic photocatalyst under ambient conditions for highly efficient synthesis of hydrogen peroxide. Proc. Natl Acad. Sci. USA 119, e2202913119 (2022).
- Ran, L. et al. Engineering single-atom active sites on covalent organic frameworks for boosting CO₂ photoreduction. J. Am. Chem. Soc. 144, 17097–17109 (2022).

- Chen, Z. et al. Tuning excited state electronic structure and charge transport in covalent organic frameworks for enhanced photocatalytic performance. *Nat. Commun.* 14. 1106 (2023).
- Fang, X. et al. Single Pt atoms confined into a metal-organic framework for efficient photocatalysis. Adv. Mater. 30, 1705112 (2018).
- Liu, R. et al. Linkage-engineered donor-acceptor covalent organic frameworks for optimal photosynthesis of hydrogen peroxide from water and air. *Nat. Catal.* 7, 195–206 (2024).
- Luo, R. et al. Singlet oxygen-dominated non-radical oxidation process for efficient degradation of bisphenol A under high salinity condition. Water Res. 148, 416–424 (2019).
- Zeng, Z. et al. Energy-transfer-mediated oxygen activation in carbonyl functionalized carbon nitride nanosheets for high-efficient photocatalytic water disinfection and organic pollutants degradation. Water Res. 177, 115798 (2020).
- 50. Ye, Y., Feng, Y., Bruning, H., Yntema, D. & Rijnaarts, H. H. M. Photocatalytic degradation of metoprolol by TiO₂ nanotube arrays and UV-LED: Effects of catalyst properties, operational parameters, commonly present water constituents, and photo-induced reactive species. Appl. Catal. B Environ. 220, 171–181 (2018).
- Lee, Y.-J. et al. Photocatalytic degradation of neonicotinoid insecticides using sulfate-doped Ag₃PO₄ with enhanced visible light activity. Chem. Eng. J. 402, 126183 (2020).
- 52. Liu, F. et al. Covalent organic frameworks for direct photosynthesis of hydrogen peroxide from water, air and sunlight. *Nat. Commun.* **14**, 4344 (2023).
- Zhou, P. et al. Single-atom Pt-l₃ sites on all-inorganic Cs₂Snl₆ perovskite for efficient photocatalytic hydrogen production. *Nat. Commun.* 12, 4412 (2021).
- Guo, X. et al. Tackling the activity and selectivity challenges of electrocatalysts toward the nitrogen reduction reaction via atomically dispersed biatom catalysts. J. Am. Chem. Soc. 142, 5709–5721 (2020).
- 55. Yan, Z., Liu, X., Ding, B., Yu, J. & Si, Y. Interfacial engineered superelastic metal-organic framework aerogels with van-der-Waals barrier channels for nerve agents decomposition. *Nat. Commun.* **14**, 2116 (2023).
- Liu, F. et al. Tunable covalent organic frameworks with different heterocyclic nitrogen locations for efficient Cr(VI) reduction, Escherichia coli disinfection, and paracetamol degradation under visible-light irradiation. *Environ. Sci. Technol.* 55, 5371–5381 (2021).
- 57. Zhang, H. et al. Different reaction mechanisms of SO₄- and •OH with organic compound interpreted at molecular orbital level in Co(II)/peroxymonosulfate catalytic activation system. *Water Res.* **229**, 119392 (2023).
- Parida, V. K., Srivastava, S. K., Chowdhury, S. & Gupta, A. K. Facile synthesis of 2D/OD Bi₂O₃/MnO₂ Z-scheme heterojunction for enhanced visible light-assisted photocatalytic degradation of acetaminophen. *Chem. Eng. J.* 472, 144969 (2023).
- Ling, C. et al. Sulfide-modified zero-valent iron activated periodate for sulfadiazine removal: Performance and dominant routine of reactive species production. Water Res. 220, 118676 (2022).

Acknowledgements

This work was supported by the National Natural Science Foundation of China under Grant No. 42025706 (to M.T.) and 52270015 (to M.T.).

Author contributions

M.T. and Y.H. designed the research. Y.H. and P.Z. performed the research with the help of K.T., Y.L., and Z.L. Y.H., P.Z., F.L., and M.T. wrote the paper. J.L. and P.Z. provided ideas. All the co-authors contributed to the interpretation of the findings.

Competing interests

The authors declare no competing interests.

Additional information

Supplementary information The online version contains supplementary material available at https://doi.org/10.1038/s41467-024-51878-6.

Correspondence and requests for materials should be addressed to Meiping Tong.

Peer review information *Nature Communications* thanks the anonymous reviewers for their contribution to the peer review of this work. A peer review file is available.

Reprints and permissions information is available at http://www.nature.com/reprints

Publisher's note Springer Nature remains neutral with regard to jurisdictional claims in published maps and institutional affiliations.

Open Access This article is licensed under a Creative Commons Attribution-NonCommercial-NoDerivatives 4.0 International License, which permits any non-commercial use, sharing, distribution and reproduction in any medium or format, as long as you give appropriate credit to the original author(s) and the source, provide a link to the Creative Commons licence, and indicate if you modified the licensed material. You do not have permission under this licence to share adapted material derived from this article or parts of it. The images or other third party material in this article are included in the article's Creative Commons licence, unless indicated otherwise in a credit line to the material. If material is not included in the article's Creative Commons licence and your intended use is not permitted by statutory regulation or exceeds the permitted use, you will need to obtain permission directly from the copyright holder. To view a copy of this licence, visit http://creativecommons.org/licenses/by-nc-nd/4.0/.

© The Author(s) 2024